Electronic Supplementary Information

Controlling the phase and morphology of amorphous Se nanoparticles: Their prolonged stabilization and anticancer efficacy

I. Experimental Section

(i) Chemicals: High purity chemicals, Sodium Selenite (Na_2SeO_3), 2, 2'-azinobis (3-ethylbenzothiazoline-6-sulfonic acid) diammonium salt (ABTS), potassium persulfate ($K_2S_2O_8$) and Ascorbic acid were obtained from Sigma-Aldrich. The RTIL (1-Ethyl-3-methylimidazolium thiocyanate, [EMIM][SCN]) was purchased from IO-LI-TEC (Germany) with >98 % purity. Further purification of the RTIL was carried out by following procedure. The 10-15 g of RTIL was treated with 0.3 g of activated charcoal for 24 h at 45^{o}C. Subsequently, RTIL was extracted using Buchner funnel apparatus and kept in vacuum oven for 24 h at 65-70^{0}C. The water content in the RTIL was measured by coulometric Karl-Fischer method (using a Metrohm 831 KF Coulometer) and found to be < 0.1 wt %. The purity of the RTIL was substantiated by measuring the conductivity of the RTIL, which was measured to be 2.4 S/m. The as measured conductivity matched with the reported one, i.e., 2.1 S/m [1]. Further, NMR, FTIR and Raman spectra of the RTIL was found to match well with those reported in the literature [2, 3, 4]. Nanopure water (conductivity, 0.06 μS cm^{-1}) used for washing the precipitates, was obtained from a Millipore water purifying system. The molecular structure of the as-employed RTIL is shown in Fig.S1 along with the denotations of various atoms of the cation and the anion.

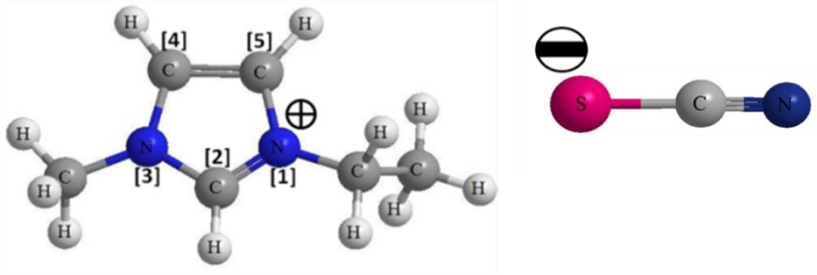

Fig.S1. Structure of ionic liquid, 1-Ethyl-3-methylimidazolium thiocyanate ([EMIM][SCN]).

(ii) Synthesis: Se nanoparticles (NPs) with tunable morphologies and phase were synthesized by a highly facile method described as follows. Na_2SeO_3 (138.5 mg) was added to 4 mL of RTIL. Subsequently, a flask containing the solution was kept in a pre-heated oil bath at 35^{o}C with simultaneous vigorous stirring for 8-10 h. This resulted in the appearance of brick red colour indicating the formation of amorphous phase Se NPs [5-7]. The precipitates were extracted by centrifugation followed by washing with ultrapure water for at least 3 times and utilized for carrying out various compositional and morphological characterization studies. Similarly, in another set of experiments, a flask containing the RTIL and Na_2SeO_3 (same concentration as mentioned earlier) was kept in a pre-heated oil bath at 70 and 120^{0}C with simultaneous vigorous stirring. The time duration of stirring at 70^{0}C was ~ 1 h, while it was 15-20 min in case of heating at 120^{o}C. These times indicate the appearance of red colour in the solution, whose intensity increased with the reaction temperature (see inset of Fig.1) at which the synthesis was carried out. The precipitates were extracted and washed by the same procedure as mentioned above. The colour difference at different temperature clearly signifies the formation of Se NPs with different morphology and phase. This was evident from the various characterization studies as discussed in the manuscript.

(iii) Reusability of the RTIL: The RTIL once used for the synthesis of the Se NPs was explored to be reused for the synthesis of next batches of Se NPs. As mentioned already, the NPs were extracted by centrifugation. At this stage, the supernatant obtained would comprise

of RTIL along with unreacted precursors as well as small quantity of un-extracted NPs. To purify the RTIL, same procedure was followed as has been mentioned earlier. Briefly, 10-15 g of RTIL was treated with 0.3 g of activated charcoal for 24 h at 45^{o}C. Subsequently, RTIL was extracted using Buchner funnel apparatus and kept in vacuum oven at 65-70^{o}C for 48 hrs. The water level and the conductivity of the RTIL were measured to ensure whether its purity level was at par with the neat one. It is to be noted that the same RTIL was again reused for the synthesis of third batch of Se NPs. The NPs were extracted using the same procedure, as mentioned earlier and various characterization studies were carried out to investigate the applicability of the reused RTIL in terms of reproducibility of the results.

(iv) Antioxidant studies by ABTS Radical Scavenging Assay

ABTS free radical scavenging activity was analysed according to the following method as reported in the literature elsewhere [8, 9]. Briefly, $ABTS^{\bullet+}$ stock solution was prepared by mixing 7 mM of ABTS and 2.5 mM of potassium persulfate and incubated at room temperature in dark for 12-16 hrs. The $ABTS^{\bullet+}$ working solution (labelled as Solution A) was prepared by dilution of the ABTS•+ stock solution and nanopure water to attain 0.70-0.80 absorbance at 734 nm. The NPs stock solution was prepared by dispersing 6.68 mg (of NPs) in 0.5 ml nanopure water. Subsequently, quantities ranging from 10-50 μl of the stock solution of NPs were added to 1.8 ml working solution of $ABTS^{\bullet+}$, i.e., Solution A. Within 30 minutes of the addition of the aliquots of the stock solutions of Se NPs to the ABTS working solution, the blue-green colour of the later turned pale. This disappearance of the colour not only varied with the dose (of NPs) but also was dependent on phase and morphology of the NPs. Subsequently, the absorbance of the solutions was recorded at 734 nm.

The antioxidant abilities of the NPs were presented in terms of IC50 value (i.e. concentration of the sample required to scavenge/inhibit 50% of radicals), which was then compared with the

standard antioxidant, such as ascorbic acid in the current work. The IC50 value of ascorbic acid was determined by following the same procedure and it was found to be ~9.26 μg/ml.

(v) Characterization: Various techniques used to characterize NPs are described as follows. The optical absorption spectra were recorded at room temperature using a JASCO V-650 absorption spectrophotometer. X-ray diffraction (XRD) measurements were recorded on a Phillips X-ray diffractometer, model PW 1710 system, using a monochromatic Cu Kα source (λ = 1.54 Å). The transmission electron microscopy (TEM) images were acquired on Libra 200FE instrument. Surface and morphological characterization of as obtained NPs were carried out using both JEOL JSM-T330 SEM and Carl Zeiss Auriga field emission SEM (FESEM). The compositional analysis for the samples was performed with energy dispersive X-ray spectrometer (EDX), attached to SEM. ^{1}H NMR spectra were recorded with a Bruker Ac-200 (500 MHz) instrument. Samples were diluted with anhydrous DMSO (dimethyl sulfoxide). The FT-IR spectra were recorded using a diamond single reflectance ATR probe in an IR Affinity-1 spectrometer. Raman spectral studies were carried out on Seki's STR300 Raman spectrometer using an excitation wavelength of 532 nm from a fibre coupled diode-pumped solid-state laser (DPSS) source. The spectrograph was calibrated using the 520.5 cm^{-1} line from silicon wafer.

(vi) Cytotoxicity studies

Cell Cultures: INT-407, human intestinal epithelial cell line and A549, Human lung cancer cell line were maintained in DMEM (Dulbecco's modified Eagle's medium) (Himedia, India) supplemented with 10% fetal bovine serum (FBS), 100 units/ml penicillin and 100 μg/ml streptomycin (Himedia, India). The cells were incubated in 5% CO_2 humidified at 37°C for growth.

Assay for Se NPs cytotoxicity: Cytotoxicity of different variant of Se NPs was carried out in human normal cell line (INT-407, an intestinal epithelial cell line) as well as human cancer cell line, (A549, a lung cancer cell line) by propidium iodide staining. The morphological changes

in INT-407 and A549 cells after 72h incubation with Se NPs were visualized using an inverted microscope (Carl Zeiss, Axiovert 40 CFL, Germany) equipped with CCD camera. Microscopic observation was further validated by MTT [3-(4, 5-dimethylthiazole-2yl)-2, 5-diphenyl tetrazolium bromide] assay in the INT-407 cells only. To confirm the result obtained from the morphological changes, propidium iodide (PI) staining was performed and data was acquired by flow cytometer. In brief, 0.25 x 10^6 INT 407 OR A549 cells were seeded in 6-well plate, one day before addition of the Se NPs. After addition of 100 μg/ml Se NPs, cells were allowed to grow for 72 h at 37°C in 5% CO_2 atmosphere. These floating cells were collected and combined with the adherent cell and stained with PI-staining solution (0.5 μg/ml propidium iodide, 0.1% sodium citrate and 0.1% Triton X-100) overnight. A total of 20,000 cells were acquired in Partec flow cytometer and analysed using Flowjo Vx.07 software. The sub-G1 population (< 2n DNA content) represented the apoptotic cells / dead cells and cells having 2n-4n DNA were considered as live cells.

For performing MTT assay, INT 407 cells (5×10^3) were seeded in a 96-well plate in Dulbecco's modified Eagle's medium (DMEM) supplemented with 10 % fetal bovine serum and antibiotics (100 units/ml penicillin and 100 μg/ml streptomycin) and kept overnight in a CO_2 incubator (5% CO_2 and 95% humidity at 37°C) for attachment. The next day old medium was replaced with fresh medium with 100 μg/ml Se NPs. Four hours before completion of 72 hours of incubation, 10 μl of MTT (5 mg/ml) was added in each well, and plates were returned to the incubator. After completing the incubation, 100 μl of solubilisation buffer (10% SDS with 0.01 N HCl) was added to each well and incubated overnight at room temperature. Colour developed after the reaction was measured at 550 nm, and background absorbance was measured at 630 nm using a microplate reader (Bio-Tek Instruments, U.S.A.).

II. Notes

(i) Optical band gap determination and the nature of band gap transition

An attempt was made to ascertain the nature of the band gap of as synthesized Se NPs as follows.

According to the Tauc's equation,

$$(\alpha h\nu) = A(h\nu - Eg)^n \quad \text{.....(1)}$$

Where, A is a constant, Eg is the band gap of the material, and the exponent n depends on the type of transition. n may have values 1/2 and 2 corresponding to the direct and indirect transitions, respectively.

Rewriting equation (1) as

$$\frac{d\{ln(\alpha h\nu)\}}{d(h\nu)} = \frac{n}{(h\nu - Eg)} \quad \text{.....(2)}$$

The plot of d{ln(αhν)}/d(hν) vs. hν is shown in Fig.S2c, which indicates a divergence at an energy value. The discontinuity at a particular energy gives the approximate value of band gap and it was found to be 2.38, 1.75 and 1.72 eV for Se NPs synthesized at 35, 70 and 120°C, respectively. The transition type is then found by extrapolating the linear parts of $(\alpha h\nu)^{1/n}$ versus hν, (where n = ½ and 2) and comparing where $(\alpha h\nu)^{1/n} = 0$ for different values of n, with the approximate value of band gap from the differential curve. We found a good agreement of band gap values for n=2, indicating an indirect band gap nature of the as synthesized NPs. Similar results regarding the indirect band gap nature of Se NPs was observed by some other researchers. For instance, Rajalakshmi *et al*. [10] reported the indirect band gap nature of Se NPs synthesized by the precipitation in a viscous polymer solution. Stroyuk *et al*. [11] synthesized colloidal Se NPs *via* acidic decomposition of sodium selenosulfate. This resulted in the formation of indirect band gap amorphous Se NPs with size in the range

of 25–200 nm. Ueda *et al*. [12] fabricated Se NPs in silica substrates by ion implantation followed by thermal annealing up to 1000 °C. The Se NPs in silica were amorphous and found to have indirect band gap. However, reports are also available for the formation of direct band gap Se NPs. For instance, direct band gap Se quantum dots with a size of 2-4 nm were produced with laser irradiation by Singh *et al*. [13]. Mehta *et al*. [14] reported the synthesis of well-distributed stable direct band gap Se NPs via an aqueous micellar solution by the assistance of surfactants of two different polarities.

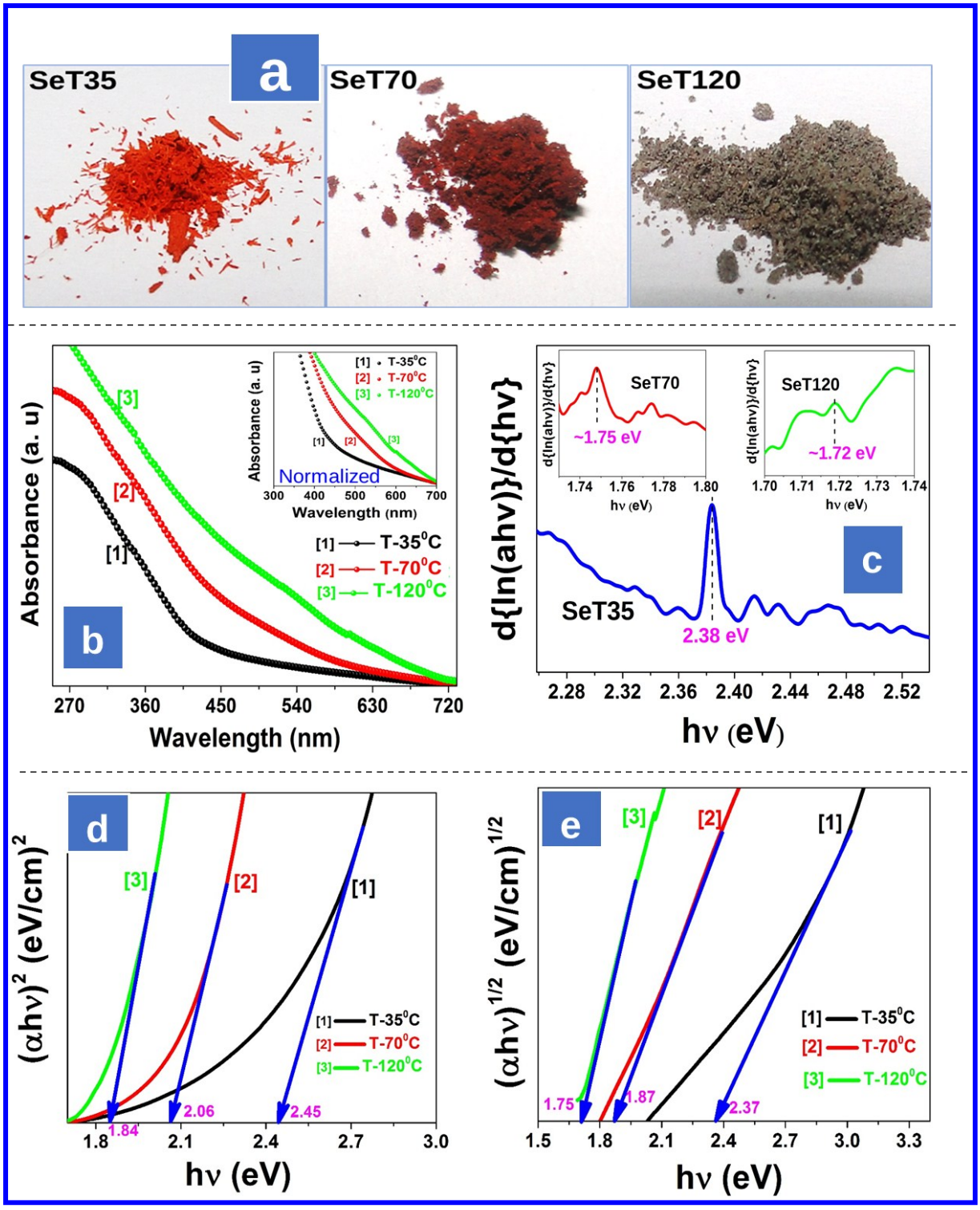

Fig.S2. (a) Camera ready pictures of Se NPs (synthesized at different reaction temperatures, i.e., SeT35, SeT70 and SeT120) extracted in the powder form. The NPs synthesized at 35°C were having brick red colour, which indicates their amorphous phase. While, the NPs synthesized at 70°C were having similar colour (as SeT35), but slightly darker appearance; suggesting bigger size than the former. The NPs synthesized at 120°C were grey in colour, which signifies their predominantly trigonal phase. (b) UV-Vis absorption spectra of Se NPs

(*extracted from the RTIL & redispersed in water*) synthesized at different temperatures. Inset shows the normalized plot. (c) The plot of d{ln(αhν)}/d(hν) vs. hν for determining the approximate value of band gap. (d) & (e) corresponds to the Tauc plot for direct and indirect band gap transitions, respectively.

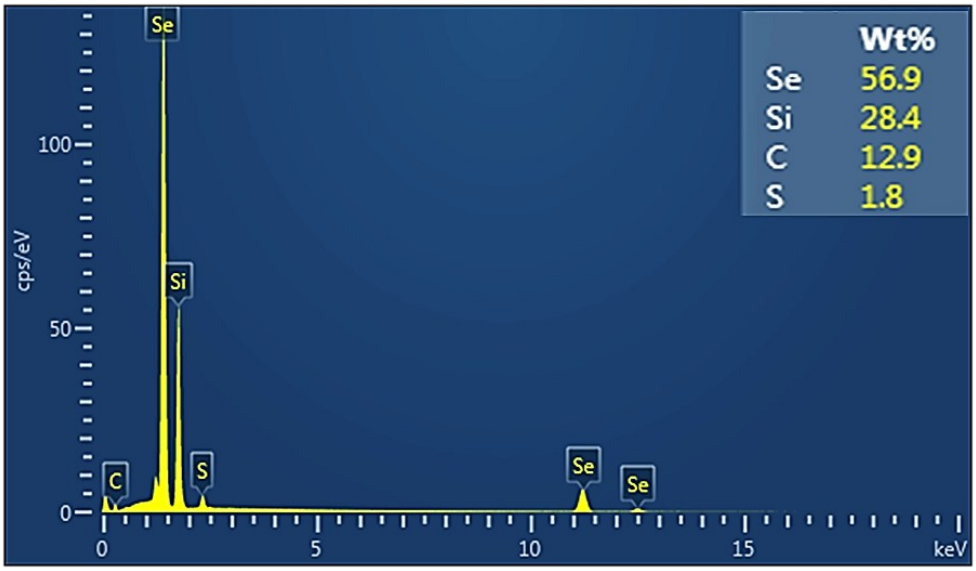

Fig.S3. A representative EDX spectrum of Se NPs.

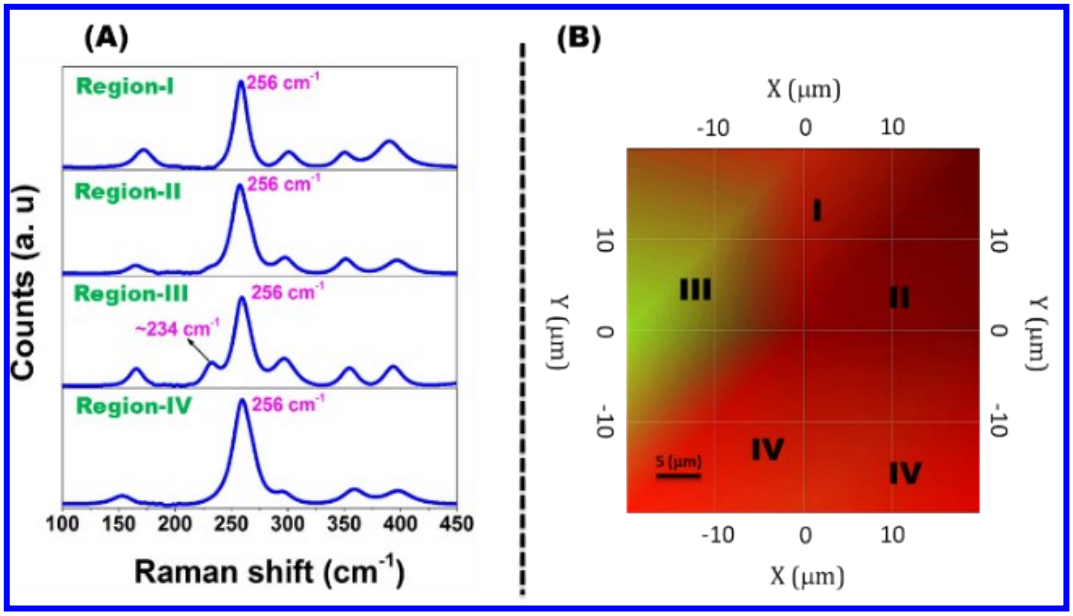

Fig.S4. (A) Representative Raman spectra of SeT35 (extracted from more than 2 month old sample) at various regions; (B) Raman image generated using phonon peak intensities. The

regions marked in the Raman image corresponds to the Raman spectra shown in panel A. The red colour corresponds to the amorphous phase, while a small green area indicates the presence of very minute crystallinity in the NPs.

(ii) Stability of Se NPs

Fig.S5 illustrates the FESEM images A & B of Se NPs (*extracted from more than 2-month-old sample*) synthesized at 35 & 70^{0}C, respectively. The morphology of the NPs still comprised of spheres or the globular nanostructures, as observed earlier. Furthermore, the average size and the polydispersity were also evaluated to ascertain the stability of the NPs. Fig.S6 shows the TEM images A & B of Se NPs (*extracted from more than 2-month-old sample*) synthesized at 35 & 70^{0}C, respectively. The diffused ring structure in the SAED pattern (shown in the inset of images A & B of Fig.S6) evidently shows the amorphous nature of the Se NPs even after time duration of more than 2 months. In addition, the particle size distributions were nearly same as observed initially. The estimated average sizes were 28±4 nm (poydispersity~14%) and 43±8 nm (poydispersity~19%), for SeT35 & SeT70, respectively.

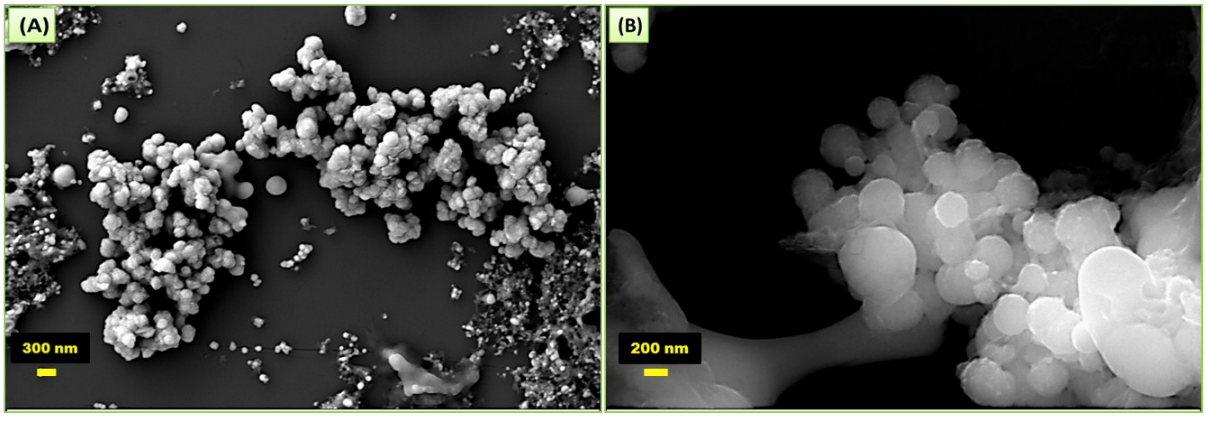

Fig.S5. FESEM images A & B of Se NPs (extracted from more than 2-month-old sample) synthesized at 35 & 70^{0}C, respectively. The nanospheres or the globular nanostructures clearly signifies the amorphous nature (or the phase stability) of the NPs.

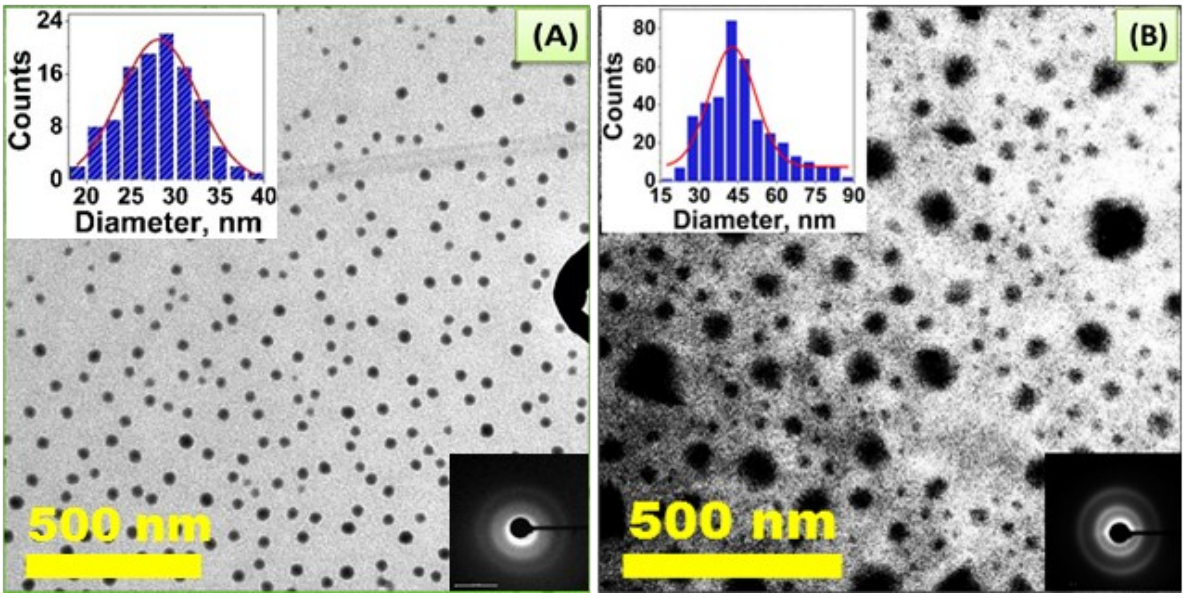

Fig.S6. TEM images A & B of Se NPs (extracted from more than 2-month-old sample) synthesized at 35 & 70^{0}C, respectively. The SAED pattern shown in the inset of images A & B shows the amorphous nature of the Se NPs even after time duration of more than 2 months. Furthermore, particle size distributions depicted in the insets of images A & B were nearly same (as were initially) for reaction conditions at 35 & 70^{0}C. The average size estimated was 28±4 nm (poydispersity~14%) and 43±8 nm (poydispersity~19%) at 35 & 70^{0}C, respectively. For comparison, the average size in case of NPs extracted immediately (mentioned earlier in the main text) after the synthesis was 24±2 nm (poydispersity~8%) and 48±4.5 nm (poydispersity~10%) at 35 & 70^{0}C, respectively. *The particle size distributions provided in the insets of their respective images were determined by measuring sizes of ~200-400 NPs. The images shown are just the representative ones and many such images of NPs recorded from various regions of TEM grids were considered for precise estimation of NP size and their distribution.*

(iii) Control Experiments: *Addition of water*

Prolonged stabilization of amorphous Se NPs was one of the important objectives of this work, which could be successfully achieved by the utilization of the host matrix of RTILs. Undoubtedly, the high viscosity as well as the strong network of intermolecular interactions in imidazolium based RTIL can be attributed to the high stability of amorphous Se NPs, which

are otherwise highly prone to spontaneous transformation to its crystalline phases. The role of high viscosity and strong intermolecular interactions of RTIL in stabilizing the NPs can be probed by manipulating these two aspects of RTIL i.e., viscosity and intermolecular interactions. One of convenient way is increasing the temperature. Apparently, with the increase in temperature, the viscosity as well as intermolecular interactions weakens. Subsequently, the phase and the morphology of the NPs can be examined in those conditions. The effect is most pronounced at 120^{o}C and leads to the formation of Se NPs with trigonal phase.

We have also performed an experiment to substantiate our claims regarding the stability of the amorphous Selenium NPs. The role of the viscosity and intermolecular interactions in RTIL in stabilizing amorphous Se NPs was further investigated by adding water into it. Apparently, the addition of water into the host matrix of RTIL would weaken the intermolecular interactions as well as lower down the viscosity. All the experimental parameters, i.e., precursor concentration and reaction temperature were maintained, as in the experiments carried out in *neat* RTIL. The reaction mixture comprised of 2 ml RTIL and 1 ml nanopure water. Subsequently, Sodium selenite (having same concentration as in case of initial *neat* RTIL based experiments) was added to the reaction mixture with simultaneous stirring, while temperature of the oil bath was maintained at 35^{o}C. Within 3-4 hrs of stirring, orange-red colour appeared which signifies the formation of Se NPs. The procedure for extraction and washing of the NPs was same as has been mentioned in the experimental section. Subsequently, the NPs were characterized. Interestingly, and as expected, the NPs were not completely amorphous, as was evident from the TEM and Raman mapping studies. The SAED pattern recorded at various regions of the sample revealed considerable presence of polycrystallinity along with the amorphous phase (see Fig.S7A). Furthermore, the NPs were found to aggregate, as can be seen in Fig.S7B. Additionally, the findings of Raman mapping also corroborated the

observations of TEM measurements. The Raman image shown in Fig.S7C clearly illustrates the presence of significant amount of crystallinity in the sample.

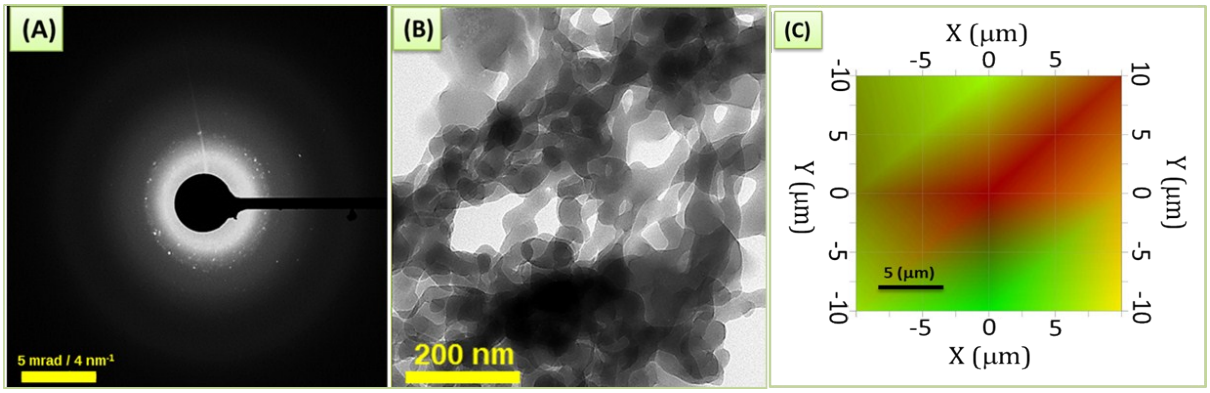

Fig.S7. (A) SAED pattern and the TEM image (B) of the Se NPs synthesized in RTIL containing water (*specifications mentioned above*). The reaction temperature was maintained at 35^{o}C. The dotted ring pattern signifies the presence of polycrystallinity in the sample. (C) Raman image generated using phonon peak intensities. The red colour corresponds to the amorphous phase, while a green area indicates the presence of crystallinity in the NPs.

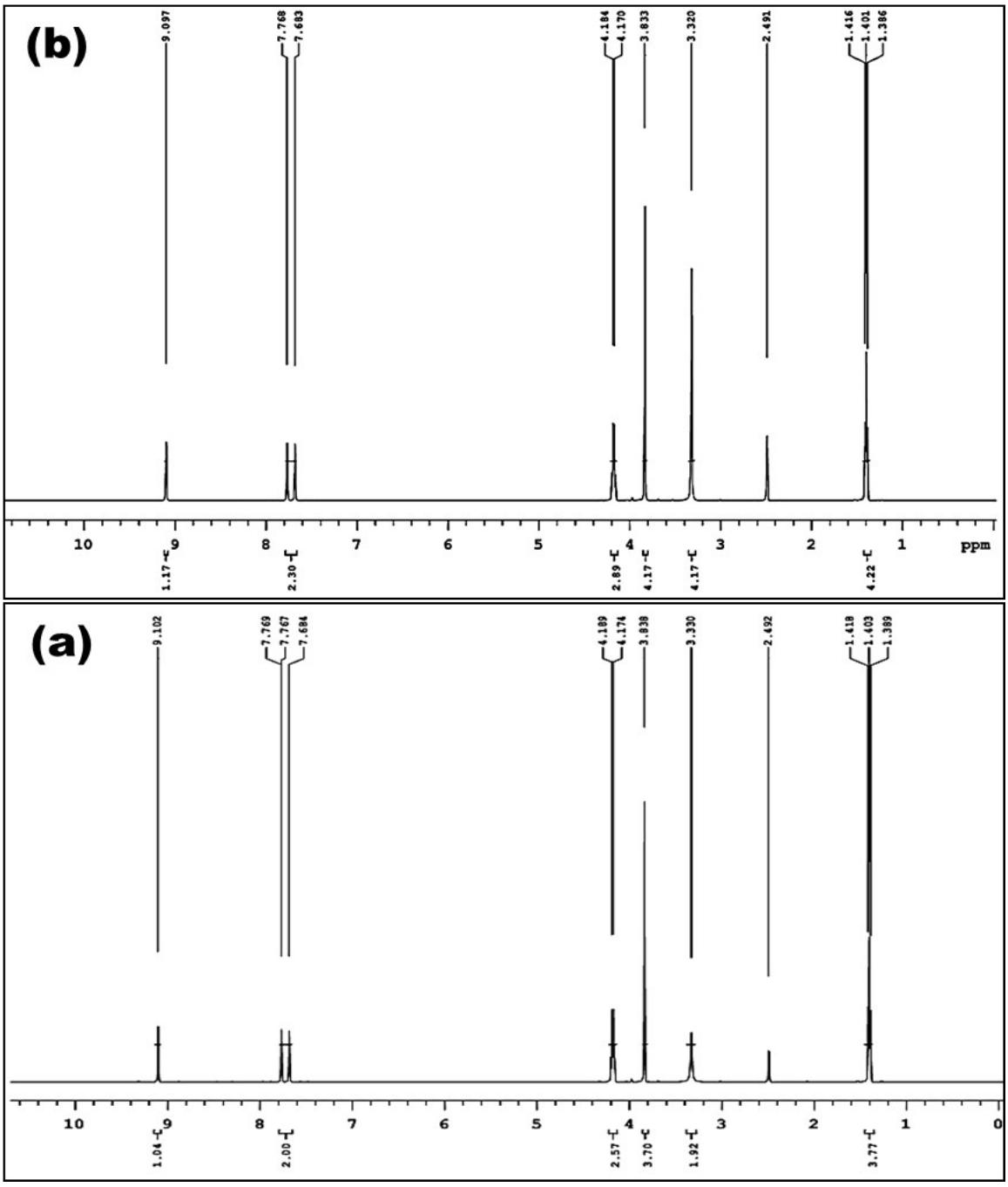

Fig.S8. [1]H-NMR spectra of neat (a) [ref 2 & 3] and reused (twice & purified) RTIL (b). The peaks at 2.4 and 3.3 ppm can be attributed to the solvent residual peaks.

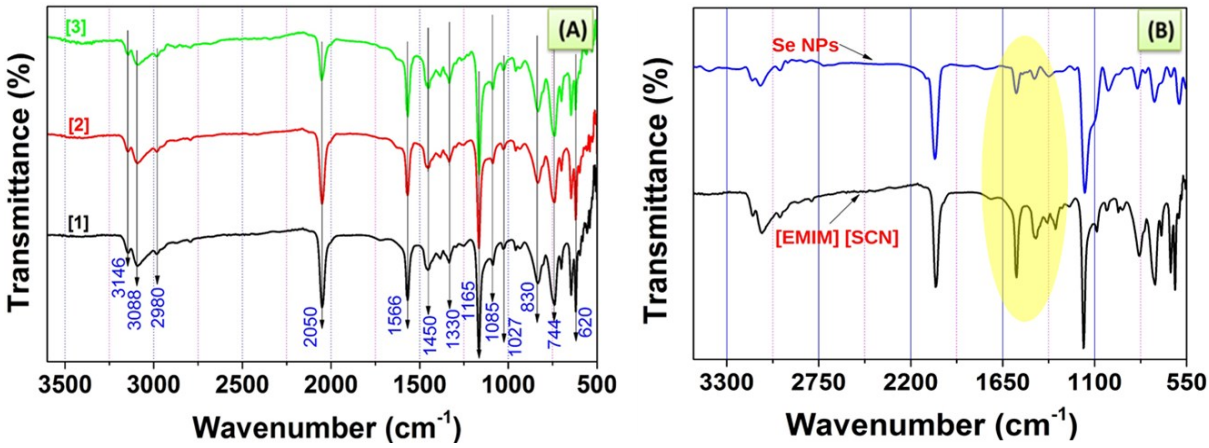

Fig.S9. (A) FTIR spectra of neat (1), once reused (2) and twice reused (3) RTIL. The peaks between 2800 and 3000 cm^{-1} originate from the ethyl chain attached to the imidazolium ring, while features between 3000 and 3200 cm^{-1} are attributed to the CH vibration modes of the imidazolium ring [3, 15]. A peak at ~2050 cm^{-1} corresponds to the anion C≡N stretching mode. Peaks at 1450 and 1566 cm^{-1} can be assigned to the imidazolium ring C=C stretching vibration, while CH3(N)CN stretching is marked by the presence of peak at 1330 cm^{-1}. Peak at 1165 cm^{-1} is attributed to the Imidazolium ring C−H deformation vibration. The peak at ~744 cm^{-1} is a signature of C-S stretching. The peaks at ~620 and 830 cm^{-1} can be attributed to the ring out-of-plane antisymmetric and ring NC(H)N bending modes, respectively [15]. The vibrational modes CH_3(N) and ring in-plane symmetric stretching modes are characterized by the presence of peaks at ~1027 and 1085 cm^{-1}, respectively [15]. **(B)** FTIR spectra of neat RTIL (i.e., [EMIM][SCN]) along with Se NPs extracted from the RTIL in the powder form. It can be seen that the FTIR of *neat* RTIL matches well with that of Se NPs extracted in the powder form. This shows the presence of RTIL molecules adsorbed on the surface of NPs. However, there are some variations in the vibrational modes of imidazolium ring, especially in the region of 1650-1300 cm^{-1} (highlighted in the spectra), which indicates closer proximity of Se NPs towards imidazolium cation than thiocyanate anion.

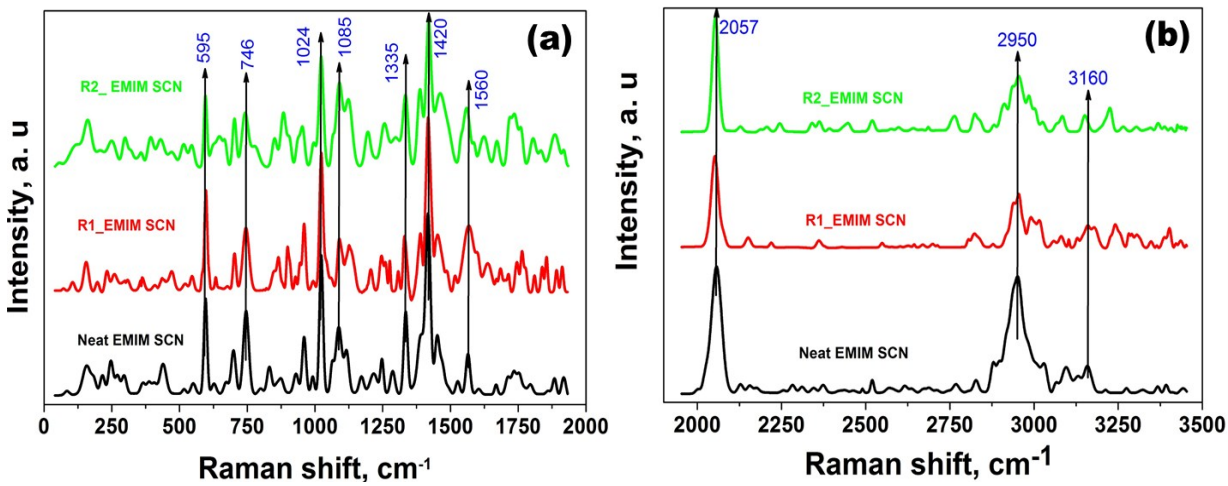

Fig.S10. Baseline corrected Raman spectra of neat, once reused (R1) and twice reused (R2) RTIL. Likewise, as in case of FTIR, the peaks between 2800 and 3000 cm^{-1} originate from the ethyl chain attached to the imidazolium ring, while features between 3000 and 3200 cm^{-1} are attributed to the CH vibration modes of the imidazolium ring [3]. A peak at ~2057 cm^{-1} corresponds to the anion C≡N stretching mode. The peak at ~746 cm^{-1} is a signature of C-S stretching. Peaks at ~1024 and 1085 cm^{-1} correspond to vibrational modes $CH_3(N)$ and ring in-plane symmetric stretching modes, respectively [15]. Imidazolium ring C=C stretching vibration modes are characterized by peaks such as 1560 cm^{-1}. The vibrational modes related to ring in-plane symmetric bend can be assigned to the peak at ~595 cm^{-1} [15].

(iv) Probable phase change mechanism of α-Se NPs and the role of RTIL

It is a well-established fact that α-Se comprises of units made of segments of chains linked to fragments of rings. However, its structure is still debated with respect to the uncertainty regarding the dominance of polymeric chains versus monomer rings [16-18].

With this brief background, the phase change mechanism of α-Se NPs can be explained by taking into account of some recent reports published by various researchers regarding the synthesis of anisotropic nanostructures of crystalline Selenium.

- For instance, Xie *et al*. [19] reported the large-Scale Synthesis and Growth Mechanism of Single-Crystal Se Nanobelts. It was observed that α-Se NPs get partially dissolved in the solution and generate free Selenium atoms, which further recrystallized and formed crystalline t-Se nuclei. The continuous feeding of Selenium atoms onto the crystalline seeds led to the formation of linear nanostructures due to the *anisotropic crystal growth*. Therefore, it was

suggested that the formation and growth of the linear nanostructures depended on the attached amorphous particles.

- Xiong *et al*. [20] reported the fabrication of single-crystalline Selenium nanoneedles. It was observed that due to higher surface free energies of a-Se seeds, a small amount of a-Se particles first converted into t-Se, which eventually resulted into the growth of wire-like nanostructures owing to the intrinsically anisotropic structure of t-Se.
- Zhou *et al*. [21] investigated the phase transition between crystalline Se (t-Se) and α-Se during the charge/discharge cycles of Li–Se battery. It is mentioned that during the amorphization process, Selenium tends to grow preferentially along the spiral chain because of the necessity to obtain a match between the highly anisotropic structure and uniaxial geometry of the one-dimensional species, as well as to favour the strong covalent bonds in helical chains over the relatively weak van der Waals forces among chains.
- Song *et al*. [22] investigated the crystallization and shape evolution of single crystalline Selenium nanorods at Liquid−Liquid Interface. It was observed by these researchers that the aggregation of α-Se nanospheres initiates the crystallization process during the growth towards nanorods.
- Mayers *et al*. [23] reported the sonochemical synthesis of trigonal Selenium nanowires. It was observed that the first step towards the formation of trigonal Selenium nanowires involved the self-assembly of the amorphous Se colloids.

Therefore, it can be realised from all these reports that one of the initial steps in the phase change mechanism of α-Se is their aggregation/ or self-assembly. This can be justified from the fact that the amorphous material is in a metastable state with respect to its crystalline counterpart, which means that the former has a higher surface-bulk ratio and higher surface free energies than the later. Apparently, it is the high viscosity and the strong network of intermolecular interactions prevailing in the RTIL, which are hindering the mobility of α-Se NPs. This was proved from the control experiments (by adding water as mentioned already) as well as by increasing the temperature. Essentially, from the FTIR (see Fig.S9B), it is clear that the RTIL molecules adsorb on the surface of NPs, thereby preventing them from coming in contact with each other. Apart from this, the presence of RTIL molecules on the surface of Se NPs was further substantiated from the Zeta potential measurements. Essentially, the Zeta potential is related to the net *surface charge* that *NPs* possess. Now, as per the findings of FTIR spectral studies, molecules of RTILs are present on the surface of NPs. RTIL being comprised of a cation and an anion, the net surface charge can be anticipated to be close to zero. Indeed,

the value of Zeta potential for the NPs redispersed in water was determined to be close to Zero. This also indicates the predominance of steric hindrance, rather than the electrostatic one, in stabilizing NPs. Moreover, the role of high viscosity as one of the major factors in the stabilization of amorphous Se NPs is further validated by the previous reports of other researchers. For instance, phase transformation of α-Se into t-Se requires ~5 h ageing period in alcohols, as reported by Gates *et al.* [24]. However, only 40–80% conversion of α-Se to t-Se over the course of 1 week was reported by *Mayers et al.* [23] for solvents with higher viscosities such as diethylene and triethylene glycol.

To summarize, based on the findings of experiments performed in the current work by varying water content and reaction temperature as well as from the previous reports, it can be said that the unique structural and the fluidic aspects of the RTILs facilitates not only the tuning of size and phase of Se NPs, but also provide a very promising facile perspective for the long term stabilization of α-Se NPs.

(v) Reuse of RTIL

Fig.S11 & S12 depicts the FESEM and TEM images of Se NPs synthesized at 70^0C using the recycled RTIL. Similar morphologies (nanospheres/or globular) can be seen from the FESEM images (Fig.S11A & B) of NPs synthesized using the same RTIL twice and thrice, respectively. Furthermore, SAED patterns shown in the inset of TEM images A & B (Fig.S12) evidently supports the amorphous nature of the NPs synthesized in the recycled RTIL as well. Additionally, NPs grown in the recycled RTIL revealed similar particle size distribution (see inset of Fig.S12A) with average particle size~42±4.8 nm (Poydispersity~11.4 %) as was observed in case of synthesis carried out first time in neat RTIL. However, NPs grown in the twice recycled RTIL showed bi-modal particle size distribution (shown in the inset of Fig.S12B) with one set of NPs predominantly with average size ~ 40 nm and other set of NPs with average size ~ 59 nm. This could be due the presence of small quantity of NPs present in

the recycled RTIL (twice), which might be acting as the seed for nucleation of the next batch of NPs leading to bigger size.

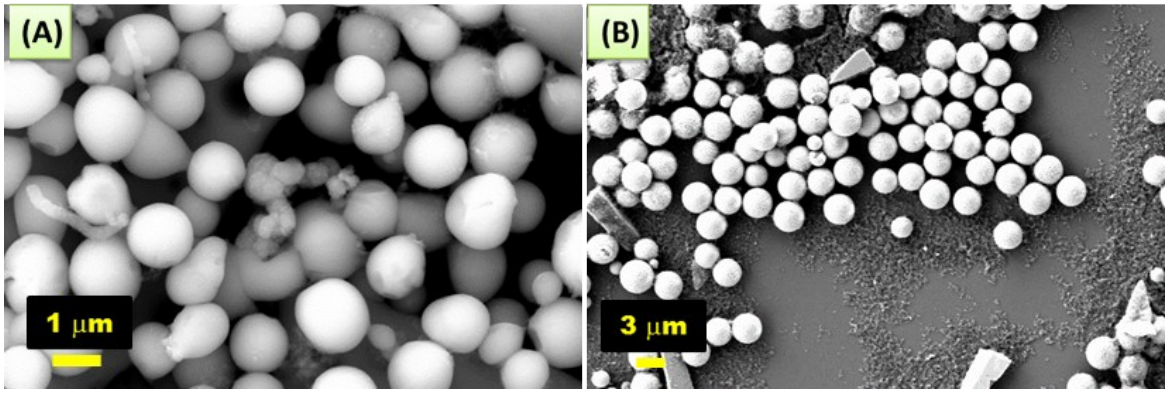

Fig.S11. FESEM images A & B of Se NPs synthesized at 70^{0}C using the same RTIL twice and thrice, respectively. The nanospheres or the globular nanostructures clearly signifies the amorphous nature of the NPs.

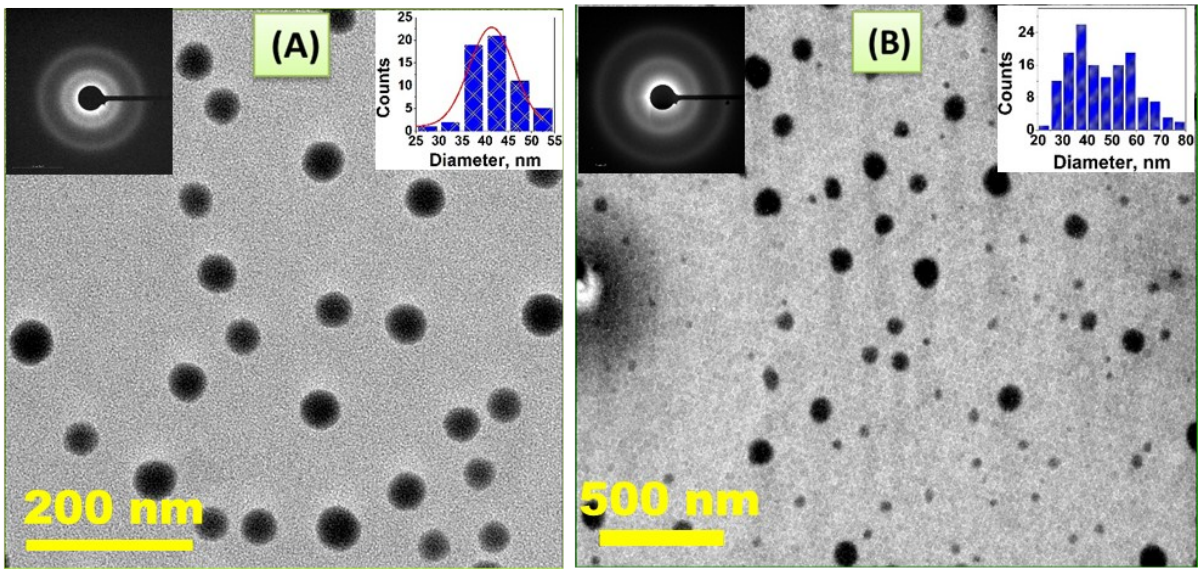

Fig.S12. TEM images A & B of Se NPs synthesized at 70^{0}C using the same RTIL twice and thrice, respectively. Inset in the images A & B depicts the SAED and the particle size distributions of the NPs. The SAED pattern shows the amorphous nature of the NPs synthesized in the recycled RTIL. The particle size distribution (42±4.8 nm; Poydispersity~11.4 %) shown in the inset of image A matches with that observed in case of synthesis carried out first time in neat RTIL (i.e., 48±4.5 nm; Poydispersity~10%). However, the particle size distribution

(shown in the inset of image B) was found to be bi-modal (one set of NPs predominantly with size of ~ 40 nm and other set of NPs with size of ~ 59 nm) in case of NPs synthesis carried out in RTIL being reused for third time. This could be due to the presence of small quantity of NPs present in the recycled RTIL, which might be acting as the seed for the next batch of NPs leading to bigger size.

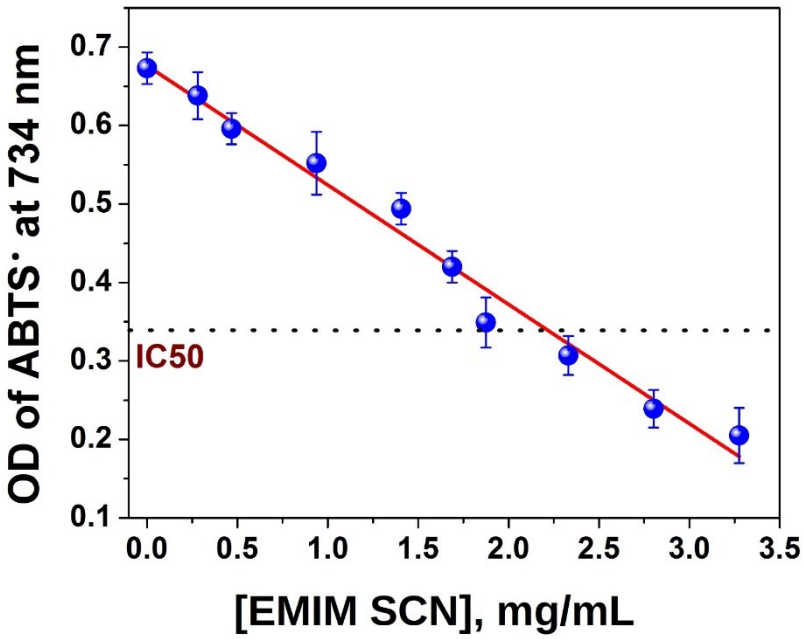

Fig.S13. Plot of [EMIM SCN] Vs. OD of ABTS radical at 734 nm. Considering the fact that RTIL possess reducing properties, a control experiment was also performed to investigate its influence on the antioxidant activity of NPs. For investigating the antioxidant activity, the NPs were extracted from the RTIL followed by washing with nanopure water (mentioned in the experimental section). Although, residual molecules of RTIL were present on the surface of NPs (as indicated from the EDX and FTIR studies) however, their influence on the antioxidant activity of NPs would be marginal, if at all. In fact, experiments performed to evaluate the antioxidant activity of RTIL revealed the same, wherein IC50 for RTIL was determined to be ~2.2 mg/ml, as can be seen from the graph. Apparently, the IC50 value of RTIL is almost 15 times higher than the IC50 value of SeT35, which clearly shows substantial difference between the antioxidant activity of Se NPs and RTIL.

(vi) Cytotoxicity Studies

Cytotoxicity studies of the Se NPs carried out in normal and cancer cells revealed interesting results. The representative images of the normal intestinal epithelial cells (shown in Fig.S14a) incubated with Se NPs (100 μg/ml) displayed almost no difference in the cell morphology with respect to the control. Flow cytometry (Fig.S14b) and MTT assay (Fig.S14c) further confirmed the considerable decrease in the toxicity of Se in nano-form. This observation is in well agreement with earlier reported findings [25, 26], where one of the probable reasons for this has been attributed to the enhancement in the activity of selenoenzymes by Se NPs, thereby causing less toxicity to the cells. Further advantage of Selenium in the nano-form is the possibility of using selenium in zero oxidation state (Se^0), which possesses low toxicity as compared to other oxidation states of Selenium (Se^{+IV}, Se^{+VI}) [26, 27]. Nonetheless, in the present work, Se NPs were also incubated in lung cancer cells, wherein, α-Se NPs (SeT35) showed toxicity, while it was least in case of SeT120 (see Fig.5b). This is evident from the fact that the normal morphology of cancer cells (i.e. adherent) significantly changes to cell shrinkage, non-adherent and round shape (see Fig.S15a). This was further confirmed from the flow cytometry studies (Fig.S15b). In this perspective, it has been shown by various researchers that the cytotoxic effects induced by Selenium compounds in tumour cells at pharmacological concentrations are primarily caused by the generation of reactive oxygen species (ROS), including superoxide. Eventually, the antioxidant defence mechanisms of tumour/cancer cells are suppressed by sustained ROS-mediated toxicity, leading to loss of structural and functional integrity, which subsequently resulted into the demise of cancer cells [28]. With this background, we have also carried out preliminary experiments based on ROS measurements to investigate the cytotoxic mechanism of as synthesized Se NPs. It was observed that incubation of the A549 cancer cells with Se NPs leads to an increase in the cellular ROS level. Further experiments are being carried out in this regard, and will be presented in future publications.

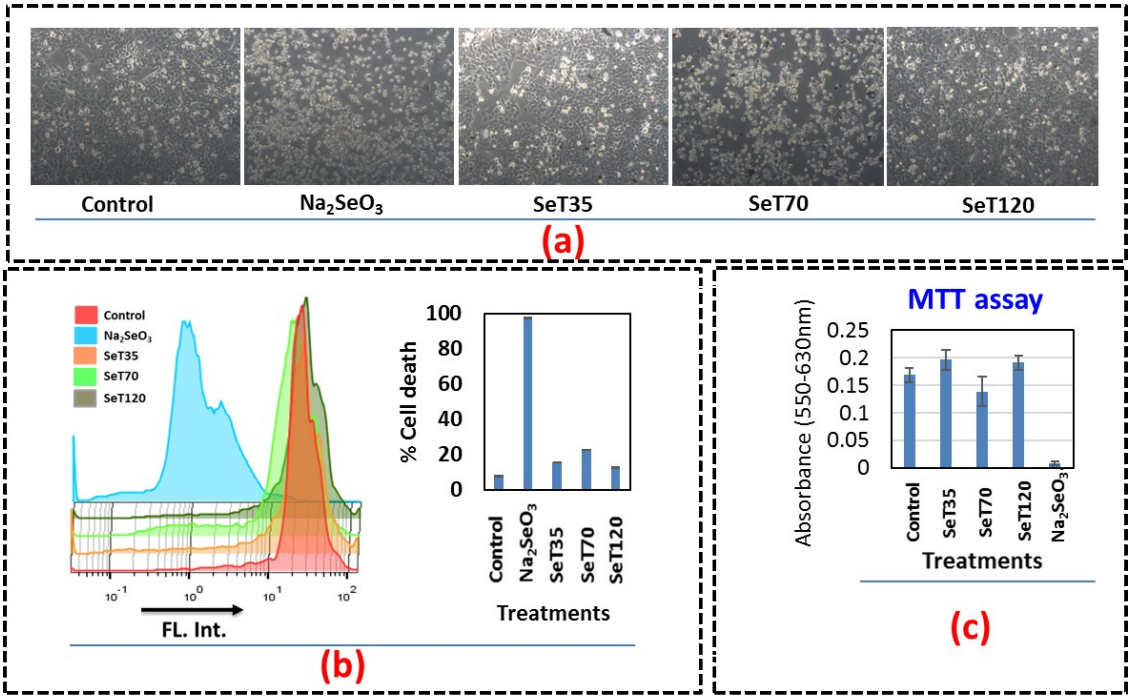

Fig.S14. (a) Morphology of INT 407, human intestinal normal cell line in presence of Se NPs synthesized at different temperatures, after 72h of incubation. (b) Flow cytometry graph and chart showing level of cell death in INT 407 cell line in presence of Se NPs. (c) MTT assay based cytotoxicity level in presence of Se NPs in INT 407 cell line.

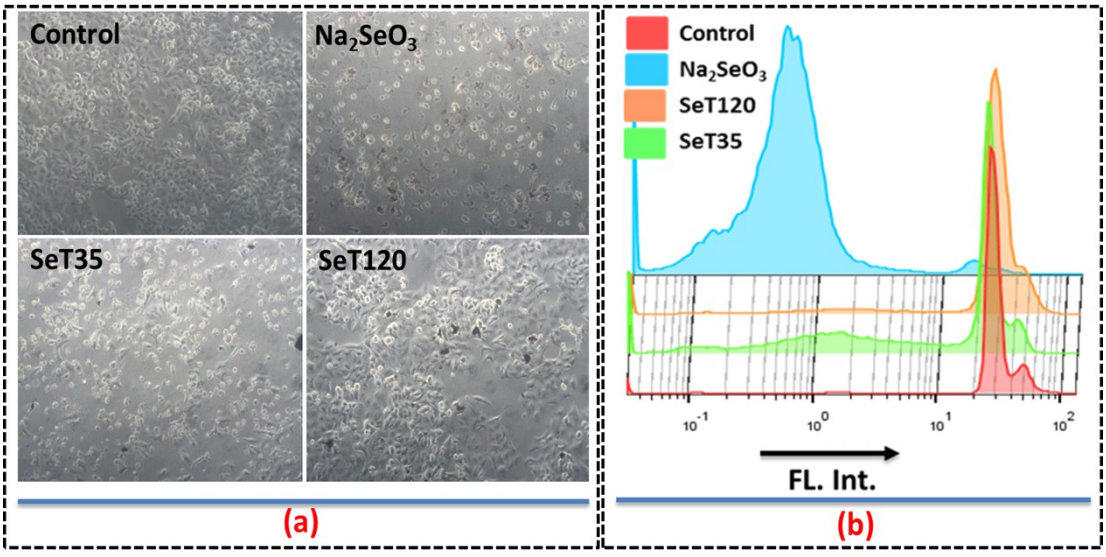

Fig.S15. (a) Morphology of A549, human lung cancer cell line in presence of Se NPs synthesized at different temperatures, after 72h of incubation, (b) Flow cytometry graph showing level of cell death in A549 cancer cell line in presence of Se NPs.

References

1. G. Sun, K. Li and C. Sun, *J. Power Sources*, 2006, **162**, 1444–1450.
2. M. Mohan, V. V. Goud and T. Banerjee, *Fluid Phase Equilib.*, 2015, **395**, 33–43.
3. Q. Zhang, M. Li, X. Zhang and X. Wu, *Zeitschrift für Phys. Chemie*, 2014, **228**, 851–867.
4. C. Y. Penãlber, Z. Grenoble, G. A. Baker and S. Baldelli, *Phys. Chem. Chem. Phys*., 2012, **14**, 5122–5131.
5. A. Guleria, A. K. Singh, S. Neogy and S. Adhikari, *Mater. Chem. Phys*., 2017, **202**, 204–214.
6. A. Guleria, S. Neogy and S. Adhikari, *Mater. Lett*., 2018, **217**, 198–201.
7. J. M. Song, J. H. Zhu and S. H. Yu, *J. Phys. Chem.* B, 2006, **110**, 23790–23795.
8. B. Yu, P. You, M. Song, Y. Zhou, F. Yu and W. Zheng, *New J. Chem.*, 2016, **40**, 1118–1123.
9. C. Zhang, X. Zhai, G. Zhao, F. Ren and X. Leng, *Carbohydr. Polym*., 2015, **134**, 158–166.
10. M Rajalakshmi and A. K Arora, *Solid State Commun*., 1999, **110**, 75–80.
11. A. L. Stroyuk, A. E. Raevskaya, S. Ya. Kuchmiy, V. M. Dzhagan, D. R.T. Zahn and S. Schulze, *Colloids Surf A Physicochem Eng Asp*., 2008, **320**, 169–174.
12. A. Ueda, M. Wu, R. Aga, A. Meldrum, C. W. White, W. E.Collins and R. Mu, *Surf. Coat. Tech.*, 2007, **201**, 8542–8546.
13. S. C. Singh, S. K. Mishra, R. K. Srivastava and R. Gopal, *J. Phys. Chem. C*. 2010,**114**,17374–17384.
14. S. K. Mehta, S. Chaudhary, S. Kumar, K. K. Bhasin, K. Torigoe, H. Sakai and M. Abe, *Nanotechnology*, 2008, **19**, 295601.
15. J. Kiefer, J. Fries and A. Leipertz, *Appl. Spectrosc.*, 2007, **61**, 1306–1311.
16. M. Marple, J. Badger, I. Hung, Z. Gan, K. Kovnir and S. Sen, *Angew. Chem. Int. Ed*., 2017, **56**, 9777–9781.
17. A. H. Goldan, C. Li, S. J. Pennycook, J. Schneider, A. Blom and W. Zhao, *J. Appl. Phys.*, 2016, **120**, 135101.

18. J. Berashevich, A. Mishchenko, and A. Reznik, *Phys. Rev. Appl*. 2014,**1**, 034008.

19. Q. Xie, Z. Dai, W. Huang, W. Zhang, D. Ma, X. Hu and Y. Qian, *Cryst. Growth Des.,* 2006, **6**, 1514–1517.

20. S. Xiong, B. Xi, W. Wang, C. Wang, L. Fei, H. Zhou and Y. Qian, *Cryst. Growth Des.*, 2006, **6**, 1711–1716.

21. X. Zhou, P. Gao, S. Sun, D. Bao, Y. Wang, X. Li, T. Wu, Y. Chen and P. Yang, *Chem. Mater*., 2015, **27**, 6730–6736.

22. J. M. Song, J. H. Zhu and S. H. Yu, *J. Phys. Chem. B*, 2006, **110**, 23790-23795.

23. B. T. Mayers, K. Liu, D. Sunderland and Y. Xia, *Chem. Mater*., 2003, **15**, 3852–3858.

24. B. Gates, B. Mayers, A. Grossman and Y. Xia, *Adv. Mater*., 2002, **14**, 1749–1752.

25. M. Gupta and S. Gupta, *Front Plant Sci*., 2016; **7**, 2074.

26. K. Bai, B. Hong, J. He, Z. Hong, R. Tan, *Int J Nanomedicine*, 2017, **12**, 4527.

27. B. Hosnedlova, M. Kepinska, S. Skalickova, C. Fernandez, B. Ruttkay-Nedecky, Q. Peng, M. Baron, M. Melcova, R. Opatrilova, J. Zidkova, G. Bjørklund, J. Sochor and R. Kizek, *Int. J Nanomedicine*, 2018, **13**, 2107–2128.

28. M. Wallenberg, S. Misra and M. Björnstedt, *Basic Clin Pharmacol Toxicol*., 2014, **114**, 377–386.